Dendrite-Free Zinc Deposition Induced by Zinc Phytate Coating for Long-life Aqueous Zinc Batteries

Leilei Du^a, Xu Hou^b, Xiaofei Yang^a, Vassilios Siozios^a, Bo Yan^b, Xiangkang Ju^b, Elie Paillard^c,

Martin Winter^{ab}, Tobias Placke^a, Jie Li^{c*}

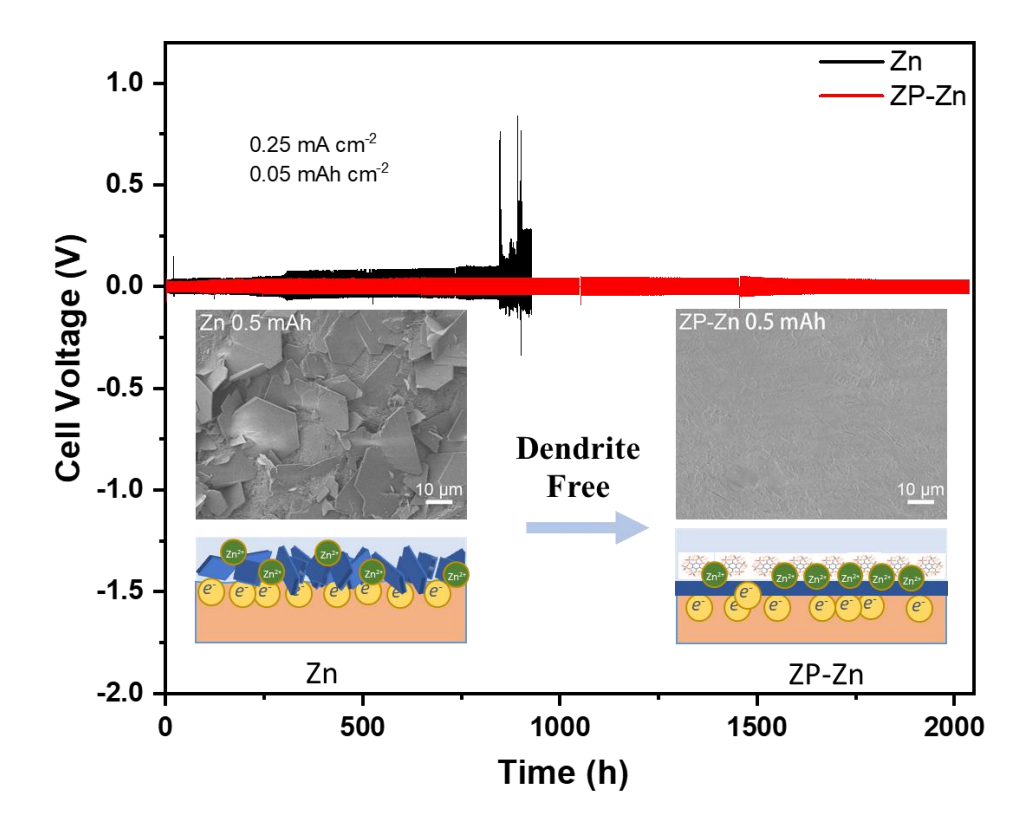
a MEET Battery Research Center, Institute of Physical Chemistry, University of Münster, Corrensstrasse 46, Münster 48149, Germany

b Helmholtz-Institute Münster (HI MS), IEK-12, Forschungszentrum Jülich GmbH, Corrensstrasse 46, Münster, 48149, Germany

c Department of Energy, Politecnico di Milano, Via Lambruschini 4, Milano, 20156, Italy

^{*} Corresponding author: Jie Li (jie1.li@polimi.it)

Graphical abstract



Highly reversible zinc plating/stripping of a Zinc Phytate modified Zinc (ZP-Zn) electrode without dendrite formation

Abstract

Rechargeable aqueous zinc batteries (AZBs) have been recognized as attractive energy storage devices because of their intrinsic superiorities, *e.g.*, high safety, low material cost and environmental benignity. However, challenges such as dendrite formation on the surface of Zn anode, poor reversibility of Zn plating/stripping and short circuit of the cell, having detrimental impact on cycle life and safety, hinder their further development. Herein, we design an artificial solid electrolyte interphase (SEI) layer for the Zn anode by coating it with a zinc phytate (ZP) layer via a facile acidetching approach. The symmetric cell with a modified Zn electrode exhibits excellent cycling stability and a low polarization voltage, since the ZP layer can guide uniform Zn deposition under the layer without dendrite formation and maintain a smooth interface between separator and electrode, which suggests Zn^2+ transport properties of the coating layer. Moreover, comparing full cells, one employing a bare Zn anode (MnO₂/carbon nanofibers (CNFs) || Zn), with the other with a modified Zn anode (MnO₂/CNFs || ZP-Zn), the MnO₂/CNFs || ZP-Zn cell delivers much better long-term cycling stability (capacity retention after 1000 cycles of 130 mAh g^{-1} vs. 50 mAh g^{-1} at a specific current of 0.5 A g^{-1}). The coating via acid etching method offers a new powerful technique for further development of practical AZBs.

1. Introduction

Nowadays, lithium-ion batteries (LIBs) have a high market share in portable electronics, electric vehicles, and even large-scale energy storage systems^[1], still there is ongoing R&D in LIBs to improve their performance, cost, safety, and environmental issues ^[2]. Alternative battery systems are another strategy to achieve more sustainable energy storage and to avoid a technology monopoly of the LIB. Significant attention has been drawn to aqueous rechargeable batteries (ARBs) with multivalent metal ions (*e.g.*, Mg, Al, and Zn, *etc.*) ^[3]. Among them, due to the inherent merits of Zn metal, such as high theoretical capacity (820 mAh g⁻¹) and low redox potential (-0.762 V *vs.* standard hydrogen electrode), aqueous zinc batteries (AZBs), especially those with mild neutral electrolyte, are particularly promising and have received numerous research interests^[3d, 4].

The Zn anode commonly suffers from low Coulombic efficiency, dendrite growth and water splitting, both in alkaline and neutral electrolytes, resulting in fast capacity fading or even short-circuits in AZBs^[5]. Besides, the formation of inactive side products (e.g., Zn hydroxides or zincates), caused by self-corrosion and hydrogen evolution reaction (HER), results in the passivation of the zinc anode surface, which is detrimental to long-term cycling^[6]. In general, the practical application of AZBs is severely restricted to the achievement of a highly reversible Zn anode^[7]. To achieve that, several strategies have been proposed and the surface modification of a Zn anode, with either inorganic compounds, polymers or carbon etc., is the most studied one. For example, a porous nano-CaCO₃ coating layer could guide uniform Zn plating/stripping rate over the entire Zn foil surface, resulting in a uniform, bottom-up Zn plating process [8]. Cui et al. [9] introduced a polyamide coating layer that elevates the nucleation barrier and restricts Zn²⁺ 2D diffusion, as well as serves as a buffer layer to isolate active Zn from bulk electrolytes, thus results in suppressed free water/O2-induced corrosion and regulated Zn deposition. Moreover, with an N-doped porous carbon coating layer, induced by the zeolitic imidazole framework (ZIF-8) [10], the Zn anode could exhibit a high Coulombic efficiency of Zn plating/stripping without dendrite formation. The complicated fabrication steps of constructing an extra layer often promote significant additional effort, which usually translates into higher costs. Thus, exploring novel methods that can achieve a uniform coating layer with improved contact between the coating material and the Zn at low efforts and cost is crucial.

Phytic acid (PA; C₆H₆(H₂PO₄)₆), extracted from natural grains and seeds, has been widely investigated as a non-toxic corrosion inhibitor to protect metal surfaces^[11] because of its powerful chelating capability with metal ions (*e.g.*, Zn²⁺, Fe²⁺, Mg²⁺). Inspired by this, zinc phytate (ZP) is considered to be an effective compound for a protective layer that can result in uniform Zn deposition and suppresses the HER on the electrode surface. More interestingly, since PA itself is an acid with phosphate carboxyl groups, it can etch the surface of Zn foil and cause the release of Zn²⁺ ions, which then chelate with PA and form a ZP layer on the Zn electrode surface. The morphology and the thickness of the coating layer is speculated to be easily changed by varying the concentration of PA solution and the reaction time. Herein, a uniform ZP coating layer is successfully fabricated through a simple and controllable way, *i.e.*, by employing a diluted PA solution to the Zn foil surface. The composition, surface morphology and electrochemical properties of the modified Zn electrode are systemically investigated. This work depicts the application of corrosion inhibitors with acidic pH as a new strategy to address the Zn dendrite issue for AZBs.

2. Results and Discussion

Figure 1 shows the morphology, hydrophilicity and structure of Zn and ZP-Zn electrodes. After etching, as observed in SEM images, the shiny surface of bare Zn foil (before in contact with PA, **Figure 1a1**) is covered by a smooth film (**Figure 1a2**). This film results in an improved wettability of the Zn electrode by the electrolyte (**Figure 1b**), which would be beneficial for the more homogenous distribution of current density on the electrode surface during electrochemical cycling. Thus, the impedance in the cell with ZP-Zn electrode is expected to be reduced. The (crystalline) structures of ZP powder, pristine and modified Zn electrodes were then characterized by XRD, and the patterns are shown in **Figure 1c**. Pristine and ZP-Zn electrodes show the same position of all reflections, meaning that the modification does not significantly impact the Zn structure. The absence

of other impurity reflections also proves that no newly crystalized phases have been formed during chemical etching. No reflections are observed in the pattern of ZP powder, indicating the amorphous structure of it. Therefore, FTIR was further used to confirm the surface components, and the spectra are displayed in **Figure 1d**. The characteristic bands of ZP, *i.e.*, at 1084 1135 and 1635 cm ⁻¹, are assigned to the stretching vibration modes of PO₄³⁻, H₂PO₄⁻ and HPO₄³⁻ [11a, 12], respectively. Those bands can be clearly observed in the spectra of ZP powder and ZP-Zn but not in the one for the pristine Zn electrode, proving that the surface layer is composed of ZP.

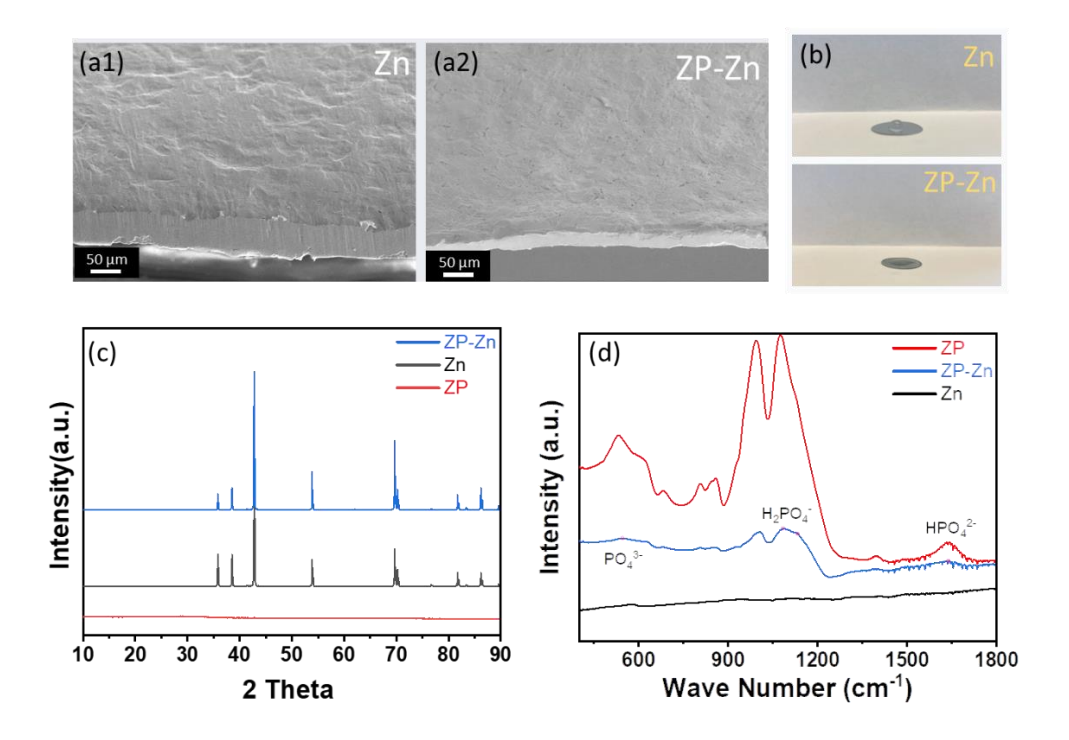


Figure 1. (a) SEM images of the bare Zn and ZP-Zn discs. (b) Optical images of bare Zn and ZP-Zn discs when adding a drop of 2 mol L⁻¹ ZnSO₄ and 0.2 mol L⁻¹ MnSO₄ aqueous electrolyte on top. (c) XRD patterns and (d) FTIR spectra of ZP powder (red), bare Zn foil (black) and ZP-Zn electrodes (blue).

The electrochemical behavior of the Zn electrode before and after PA modification was first compared in symmetric cells, as shown in **Figure 2**. The cells were galvanostatically cycled at 0.25 mA cm⁻² with a limitation of the areal capacity of 0.05 mAh cm⁻². The charge transfer resistances before cycling in both cells are much higher than those after the 1st cycle, revealed by the impedance measurement (**Figure S1**), indicating the existence of the activation process during the initial cycle. Both cells behave low overvoltage in the early period of cycling, *e.g.*, 69 mV for the Zn \parallel Zn cell and 53 mV for the ZP-Zn \parallel ZP-Zn cell (left inset of **Figure 2**) after 50 hours, while after 300 h, the

nucleation overvoltage in the ZP-Zn || ZP-Zn cell increases much slower in comparison with the Zn || Zn cell. For example, the Zn || Zn cell exhibits an overvoltage of 124 mV after 500 hours (right inset of **Figure 2**), while the value of the ZP-Zn || ZP-Zn cell is only 72 mV. This fast increase in the Zn || Zn cell may attribute to a fast accumulation of Zn dendrites as well as the formation of zinc hydroxide sulfate (Zn(OH)₂)₃(ZnSO₄)·₅H₂O; ZHS) on the surface of bare Zn. Since the loose and messy ZHS layer would deteriorate the electrochemical performance^[13] of a zinc-based cell, a much larger polarization and micro short-circuit formation can be observed in the cell with the bare Zn electrode after 900 hours (**Figure S2a**). In contrast, the cell with ZP-Zn electrode displays an excellent stripping/plating behavior even after 2000 hours or 5000 cycles (**Figure S2b**). When increasing the current density to 25 mA cm⁻² (**Figure S3**), the cell with ZP-Zn electrodes shows better reversibility and lower nucleation overvoltage than the Zn || Zn cell throughout the whole measurement period. Both results demonstrate that the PA-modified electrode can enable stable and rapid Zn stripping/plating for a much longer term, which could be attributed by the presence of the ZP coating layer.

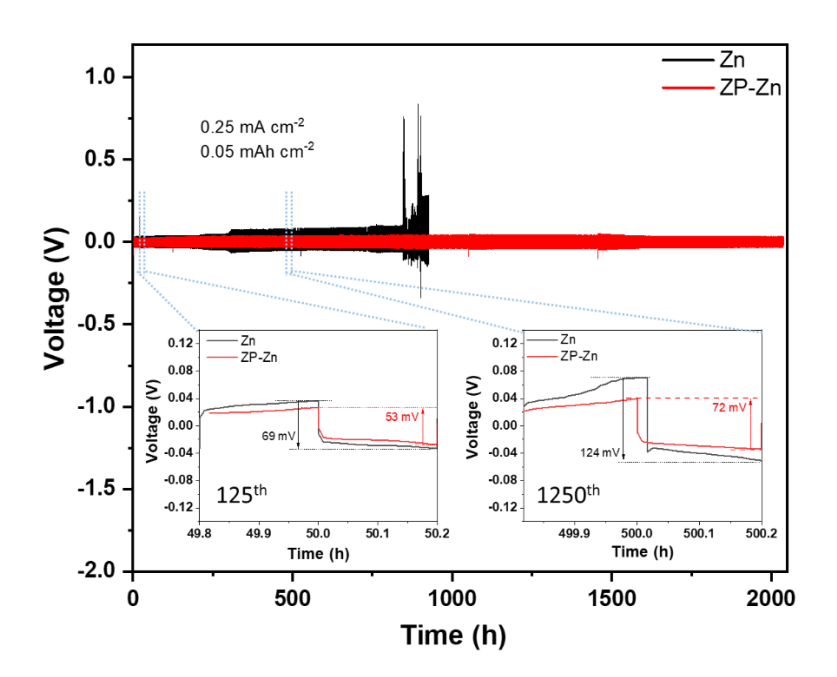


Figure 2. Galvanostatic Zn stripping/plating in symmetric cells with either bare Zn electrodes (black) or ZP-Zn electrodes (red). The cells were cycled at 0.25 mA cm⁻² with an areal capacity of 0.05 mAh cm⁻². The left inset and right inset figures are enlarged voltage-time diagrams of the 125th and 1250th cycles, respectively. In these cells, glass fiber was used as separator in combination with 2 mol L⁻¹ ZnSO₄ and 0.2 mol L⁻¹ MnSO₄ aqueous electrolyte.

To study how the ZP coating layer affects the Zn stripping/plating behavior, the surface morphology of the electrodes after Zn deposition with various capacities, *i.e.*, 0.05 mAh cm⁻², 0.1 mAh cm⁻² and 0.5 mAh cm⁻², have been characterized by SEM, and the corresponding images are shown in **Figure 3**. The surface of the bare Zn foil (**Figure 3a**) is clean and flat, but changes obviously after Zn deposition (**Figure 3b-d**). Uneven Zn deposits can be easily observed after 0.05 mAh cm⁻² capacity of Zn deposition, while the flake shaped ZHS, whose morphology agrees with previous reports [13-14], also appears simultaneously. ZHS is more pronounced by prolonging the deposition time, and almost fully covers the electrode after 0.5 mAh cm⁻² deposition. In contrast, no ZHS can be observed in the deposited ZP-Zn electrode, and the ZP-Zn surface does not show obvious changes (**Figure 3f-h**), which suggests that the deposited Zn grows under the ZP coating layer. The resulting stable interface of the Zn electrode with the electrolyte leads to a low impedance in the ZP-Zn symmetric cell (**Figure S1**) and improved long-term cycling stability (**Figure 2**). In contrast, the numerously formed ZHS as well as the Zn dendrite on the bare Zn electrode would contribute to the performance decay.

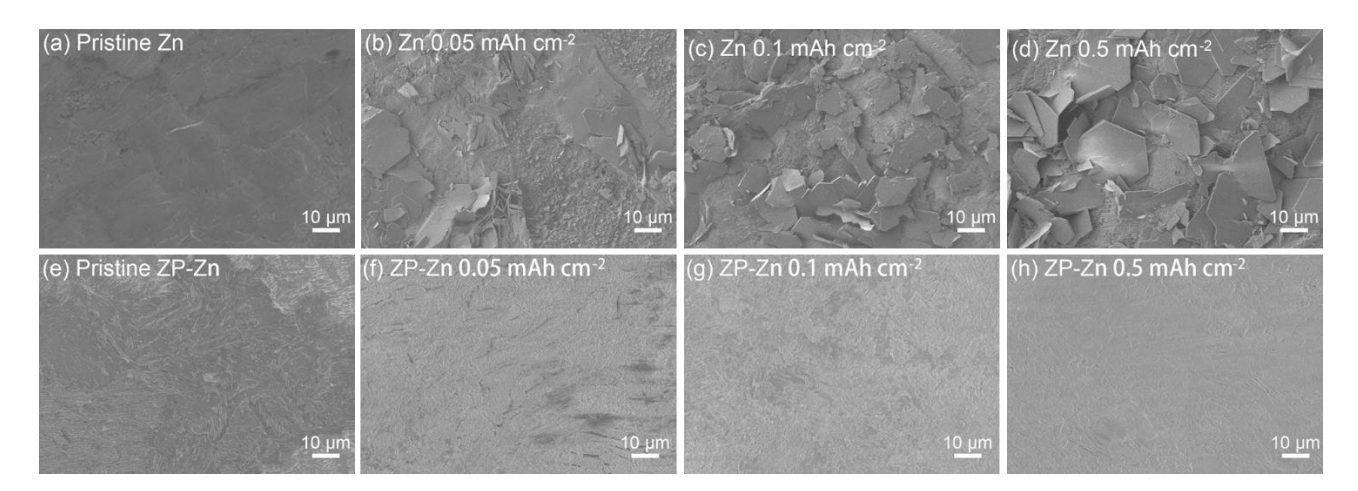


Figure 3 SEM images of bare Zn and ZP-Zn electrodes before (a & d) and after 0.05 mAh cm⁻² (b & f), 0.1 mAh cm⁻² (c & g), 0.5 mAh cm⁻² (d & h) Zn deposition capacities by charging for 0.2 hours, 0.4 hours and 2 hours at 0.25 mA cm⁻², respectively. The electrodes were taken from disassembled symmetric cells with filter paper as separator in combination with 2 mol L⁻¹ ZnSO₄ and 0.2 mol L⁻¹ MnSO₄ aqueous electrolyte.

It must be noted that no Zn dendrite or flake ZHS formation can be observed on the surface of the ZP-Zn electrode even after 0.5 mAh cm⁻² of Zn deposition, suggesting that the Zn deposition occurs under the ZP coating layer, which is further confirmed by the cross-section of SEM image and EDX

mapping of O, P and Zn, as displayed in **Figure 4a-d**. A coating layer can be seen (**Figure 4a**), which is evenly, flat, and tightly attached to the surface of Zn foil. O and P (**Figure 4b & 4c**), as the main elements in ZP, are only observed on the electrode surface after Zn deposition, which clearly demonstrates the location of deposited Zn, *i.e.* under the ZP layer and directly on the bare Zn substrate. This further suggests that the ZP coating layer has Zn²⁺ transport properties.

Even after 50 cycles, as shown in **Figure 4e & 4f**, different from the bare Zn electrode that having stacked ZHS formed on the surface, ZP-Zn maintains the clean and flat surface, though cracks appear in the ZP layer, which is probably due to repeated Zn plating/striping. Nevertheless, its upside surface keeps clear and excludes of ZHS formation along cycling, which explains why ZP-Zn exhibits lower nucleation overvoltage and better long-term cycling performance than bare Zn in symmetric cells independent to the deposition capacity, as displayed in both **Figure 4g** (for 0.5 mAh cm⁻¹) and **Figure 2** (for 0.05 mAh cm⁻¹). **Figure 4h** shows XRD patterns of both bare Zn and ZP-Zn electrodes after 50 cycles: New reflections appear on the bare Zn electrode, which can be assigned to the crystalized ZHS (JCPDS:78-0246) [15]. At difference, the ZHS phase cannot be seen in the pattern of ZP-Zn electrode, and all reflections have same positions as the pristine pattern (**Figure 1c**). In other words, the Zn deposition on the ZP-Zn electrode follows the simple conversion reaction (equation 1), while on the bare electrode, a complicated process of mixing the formation of ZHS (equation 2) and the conversion reaction (equation 1) occurs. The unitary Zn plating behaviour gives the answer to why the ZP-Zn electrode can keep a stable surface, which agrees with **Figure 3e-h**.

$$Zn^{2+} + 2e^- \rightarrow Zn \tag{1}$$

$$4Zn^{2+} + 6OH^{-} + SO_4^{2-} \rightarrow Zn_4SO_4(OH)_6$$
 (2)

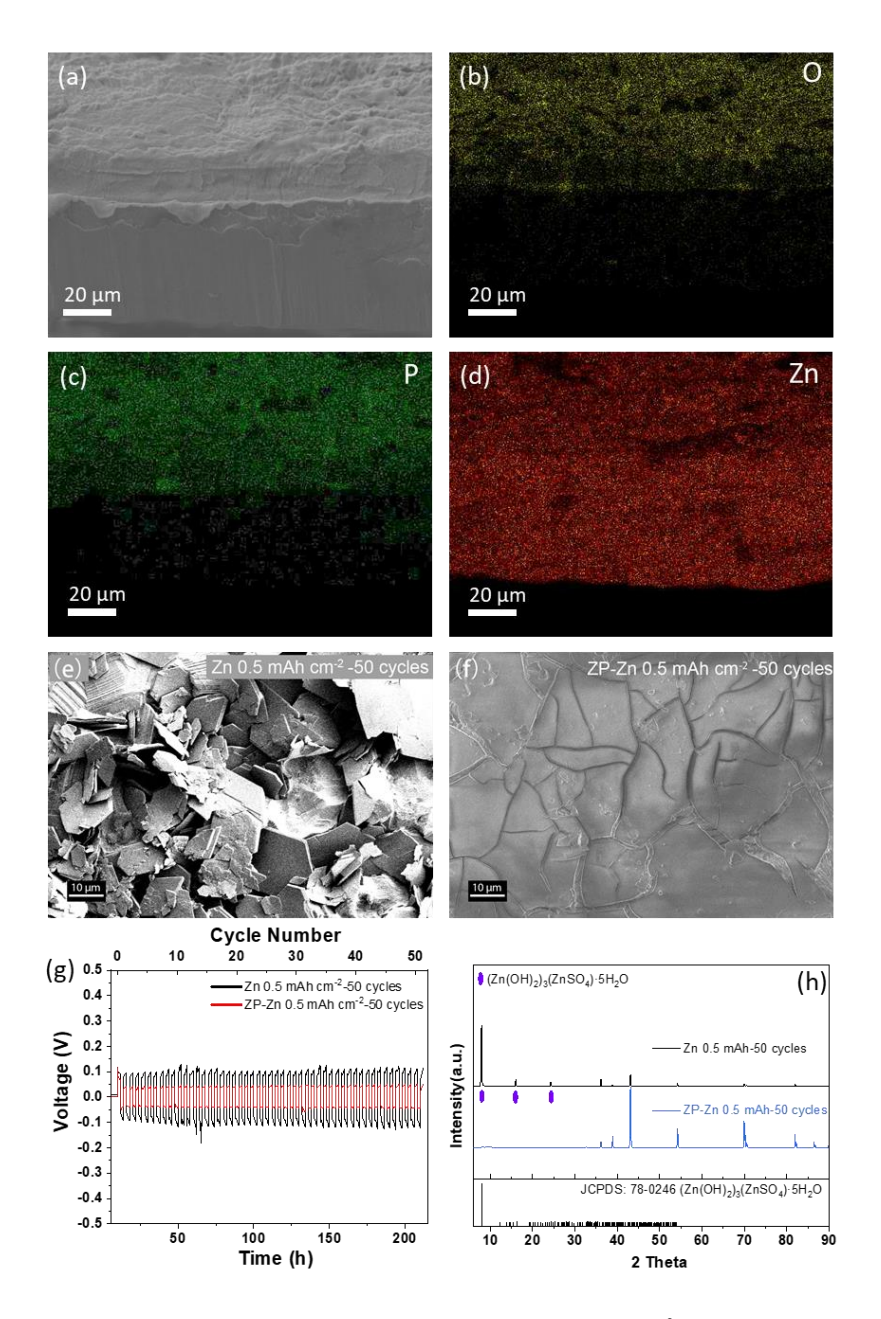


Figure 4 Cross-sectional SEM images of (a) ZP-Zn electrodes after 0.5 mAh cm⁻² Zn deposition, and corresponding EDX mapping (b-d) for O, P and Zn, respectively. SEM images of cycled (e) bare Zn and (f) ZP-Zn electrodes and (g) the corresponding voltage-time plots after 50 cycles with the capacity limitation of 0.5 mAh cm⁻². (h) XRD patterns of cycled bare Zn and ZP-Zn electrodes. All cells are symmetric cells and the filter paper was used as separator in combination with 2 mol L⁻¹ ZnSO₄ and 0.2 mol L⁻¹ MnSO₄ aqueous electrolyte.

Summarizing the above discussions, the Zn deposition process on different Zn electrodes is illustrated in **Figure 5**, a) shows bare Zn electrode and b) displays the ZP-Zn electrode. The cell bulge and the electrolyte leakage originated from hydrogen evolution, which often happens in symmetric Zn cells after long-term cycling ^[16], were also observed in this work. Thus, the gradually increased OH-concentration leads to the formation of ZHS, under the presence of SO₄²⁻ anions^[15b]. In other words,

the concentration of OH $^{\circ}$ and SO4 $^{\circ}$ strongly affects the type of products during Zn plating, *i.e.*, deposited metallic Zn, ZHS or their combination. In a cell with a bare Zn electrode, at the beginning of deposition, Zn $^{\circ}$ nucleates and plates on the Zn substance surface, following equation 1, due to the low concentration of OH $^{\circ}$. Then, side-reactions start when the deposition continues, *i.e.*, the concentration of OH $^{\circ}$ rises consequently and the flake-like ZHS appears as the product of the reaction among OH $^{\circ}$, Zn $^{\circ}$ and SO4 $^{\circ}$ (equation 2)[17]. These ZHS complexes form a loose surface layer, which results in the messy electrode surface and may even pierce the separator, thus promoting Zn dendrite formation and deteriorating the electrochemical performance of the cell.[113,18] In contrast, in terms of the ZP-Zn anode, the functional groups of H2PO4 $^{\circ}$ and HPO4 $^{\circ}$ in the ZP coating layer can neutralize OH $^{\circ}$ bonds, and therefore buffer the change of pH value of the electrolyte. This function can be confirmed by a simple experiment, *i.e.*, comparing the pH value evolution of distilled water and ZP suspension after dropping NaOH solution (0.01 mol L $^{\circ}$) gradually, and the results are shown in **Figure S4**. Although the pH value of distilled water increases directly with addition of 50 μ L NaOH solution, the pH maintains stable (< 7) in a ZP suspension till adding 200 μ L NaOH solution.

$$H_2PO_4^- + OH^- \leftrightarrow HPO_4^{2-} + H_2O$$
 (3)

$$HPO_4^- + OH^- \leftrightarrow PO_4^{3-} + H_2O$$
 (4)

The pH buffer ability is due to the existence of H₂PO₄⁻ and HPO₄²- groups (proved by FTIR spectra in **Figure 1d**) in ZP, which can consume OH⁻ ions (equation 3 and 4) originated from side reactions. The low concentration of OH⁻ sufficiently limits the formation of ZHS even after 50 cycles (**Figure 4h**). Meanwhile, the low nucleation overvoltage (**Figure 2** and **Figure 4g**) can suppress the side reactions and therefore prevent fast generation of OH⁻. Therefore, with the artificial ZP layer, a uniform Zn deposition can be achieved on the Zn electrode. Additionally, the growth of undesirable ZHS that may aggravate the impedance and even lead to cell short-circuit can be noteworthily limited.

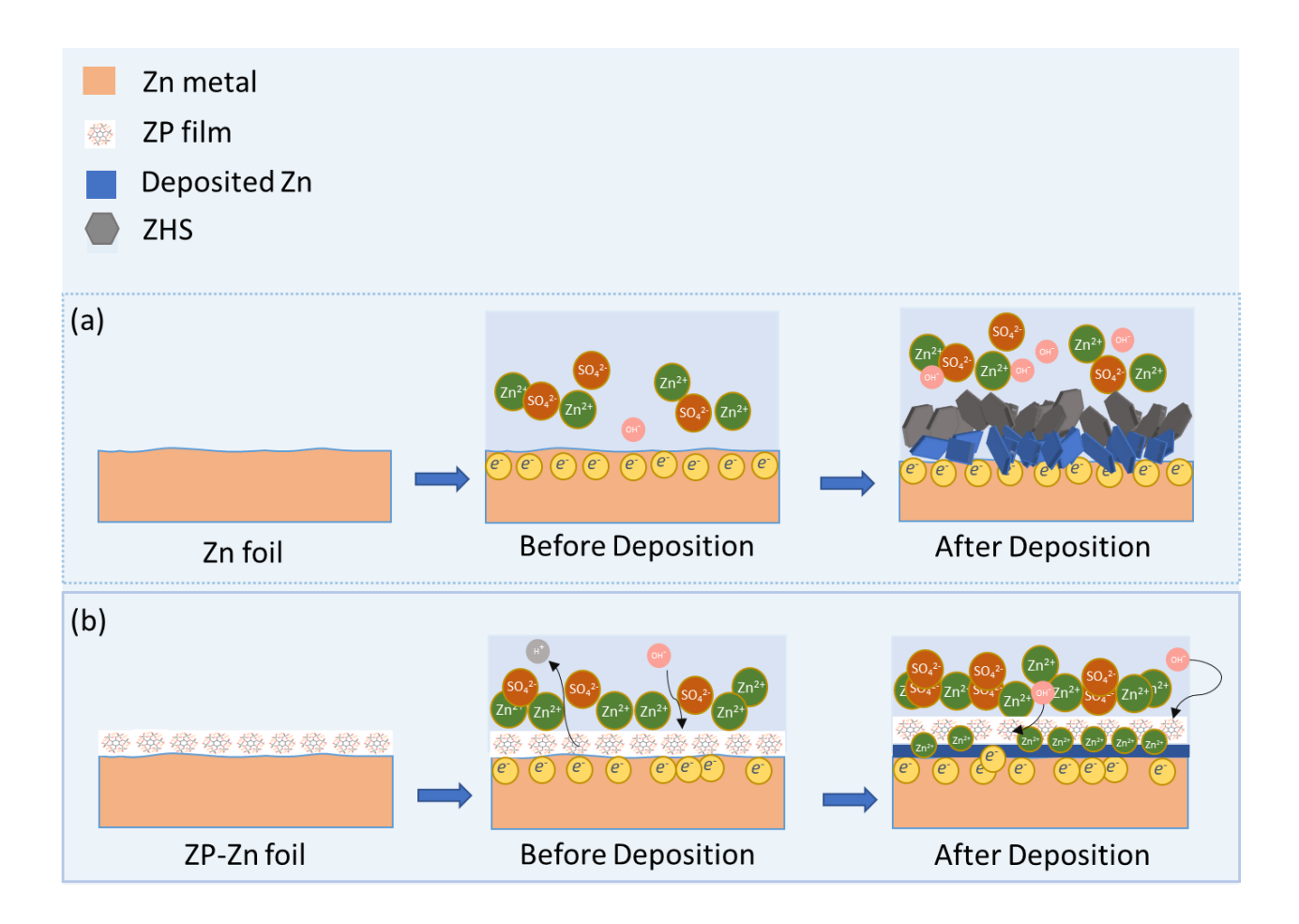


Figure 5. Schematic diagram of product evolution on bare Zn electrodes (a) and on ZP-Zn electrodes (b) during the Zn deposition process.

Last but not the least, the electrochemical performance of both Zn anodes was compared in full cells by employing MnO₂/CNFs electrodes as cathode. **Figure S5** & **S6** show the SEM images and XRD patterns of CNFs and MnO₂/CNFs, which are agree well with the previous report^[19]. **Figure 6a** exhibits the long-term cycling performance of both cells that were cycled first at low specific current of 100 mA g⁻¹ for 10 cycles and then at 500 mA g⁻¹ for 1000 cycles. Though both cells exhibit similar specific capacity of near 200 mAh g⁻¹ at 100 mA g⁻¹, MnO₂/CNFs || ZP-Zn cell delivers obviously higher capacity at 500 mA g⁻¹ and decays at much slower pace, which can be clearly seen in Figure S7 for the capacity evolution of the initial 20 cycles. This result demonstrates the enhanced rate capability of full cell with ZP-Zn electrode. After 150 cycles, it shows a capacity of 130 mAh g⁻¹ that is maintained until the end of measurement (1000 cycles). The capacity retention reaches 80.2 % in comparison with the initial value delivered at 500 mA g⁻¹ (the 11th cycle). On the contrary, the MnO₂/CNFs || Zn cell performs low specific capacities and only maintains 33.5 % after 1000 cycles.

Its relatively "bouncing" Coulombic efficiencies also indicate an instability of the Zn^{2+} plating/stripping for the bare Zn electrode. The Nyquist impedance plots of the two cells are shown in **Figure 6b** & **c**, both cells show a dramatic impedance decrease from the initial to the 10^{th} cycle because of the electrochemical activation process, which explains the growing trend in their specific capacity in the first 10 cycles. Nevertheless, $MnO_2/CNFs \parallel ZP-Zn$ cell shows obviously lower impedance than that in $MnO_2/CNFs \parallel Zn$ cell, indicating that the ZP coating layer also contributes to a lowering of the cell inner resistance and enhances the rate capability of a full cell; still an activation step is needed to achieve this $^{[20]}$.

In order to compare the redox reactions between the two cells, the CV curves obtained at 0.5 mV s^{-1} between 0.9-1.8 V are shown in **Figure 6d**. Two pairs of redox peaks can be observed in both curves which can be assigned to the redox reactions of $Mn^{4+} \leftrightarrow Mn^{3+} \leftrightarrow Mn^{2+}$ during the insertion/extraction of H^+ and/or Zn^{2+} into/out of MnO_2 cathode $^{[21]}$. The voltage gaps between the oxidation and reduction peaks are bigger in the curve of MnO_2 /CNFs \parallel Zn cell in comparison with those in MnO_2 /CNFs \parallel ZP-Zn cell , which may due to the larger cell inner resistance, as indicated in **Figure 6c**. Consistent with the CV curves, two plateaus, corresponding to the H^+ insertion (at high voltage) and Zn^{2+} insertion (at low voltage), appear in the voltage profiles of both cells (**Figure 6e**). Since the kinetics of H^+ insertion is faster than that of Zn^{2+} insertion $^{[21b]}$, the cell with a higher proportion of H^+ insertion is expected to deliver an increased capacity especially at high rates. Though both cells deliver similar discharge capacities of ~190 mAh g⁻¹, the proportion of capacity from H^+ insertion for the MnO_2 /CNFs \parallel ZP-Zn cell is higher than that of MnO_2 /CNFs \parallel Zn cell (57% vs. 50%) according to the voltage profiles in the 10^{th} cycle. This results in a better rate capability, as proven by the obvious less capacity decay when increasing the specific current from 100 mA g^{-1} to 500 mA g^{-1} .

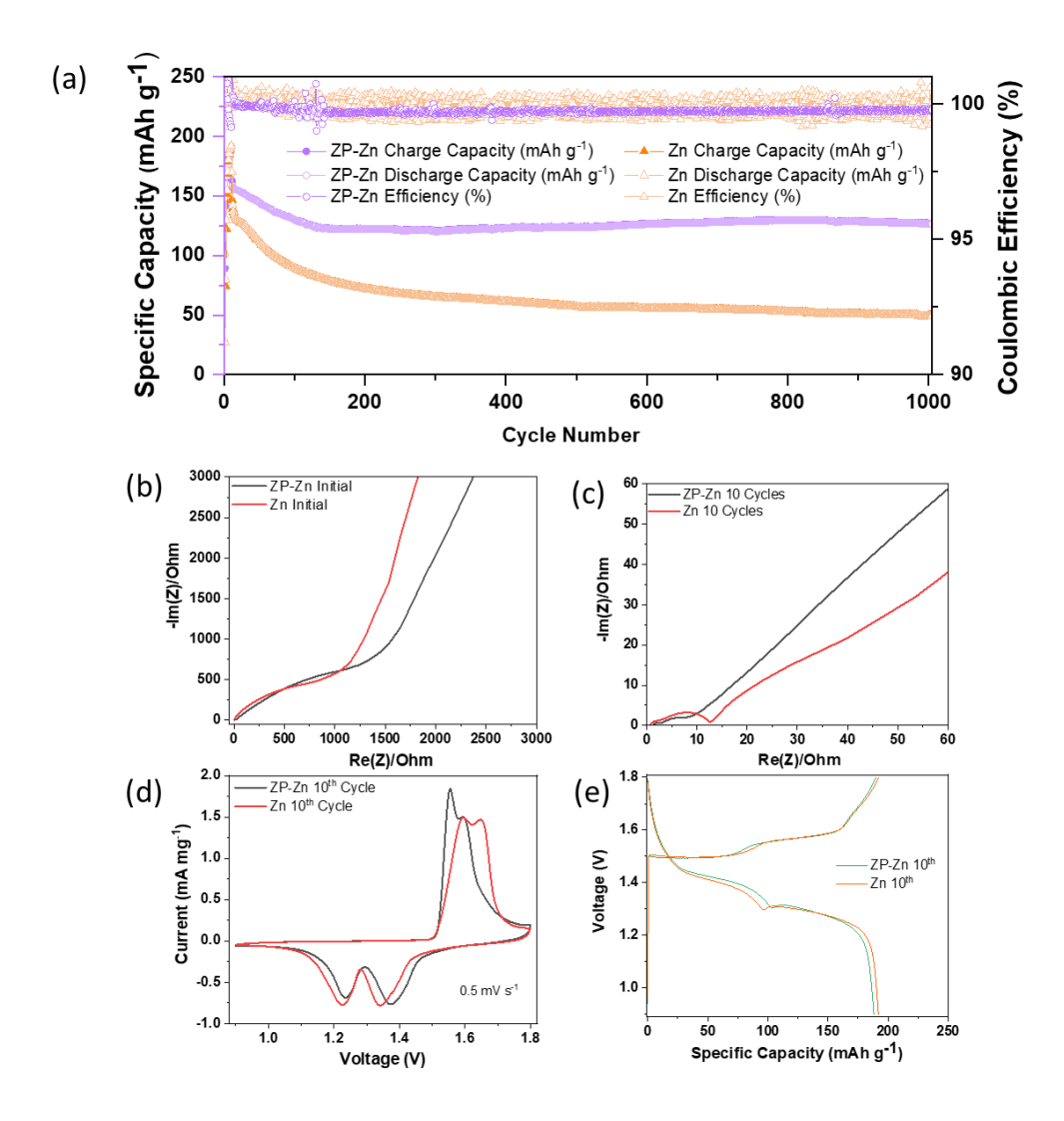


Figure 6. Electrochemical behaviour of MnO₂/CNFs || Zn and MnO₂/CNFs || ZP-Zn cells, including, (a) the galvanostatic long-term cycling performance at 500 mA g⁻¹ (the specific current is calculated according to the weight of MnO₂/CNFs composite), the EIS spectra for (b) initial state and (c) after 10 cycles, (d) the CV curve for both cells at the 10th cycle, and (e) the charge-discharge voltage curves of the 10th cycle extracted from cycling performance. Glass fiber (Whatman GF/D) was used as separator in all the cells in combination with 2 mol L⁻¹ ZnSO₄ and 0.2 mol L⁻¹ MnSO₄ aqueous electrolyte.

3. Conclusions

We propose a facile and low-cost coating strategy, *i.e.* acid etching method, to modify the Zn anode for aqueous Zn batteries. With this method, a zinc phytate (ZP) coating layer is introduced to the surface of the Zn anode, which can induce uniform Zn deposition under it and serve as protective layer to suppress side reactions leading to the formation of undesirable ZHS products. Thus, a low

nucleation overvoltage, an effective electrode|electrolyte interface and delayed electrolyte decomposition, enabled by the ZP coating, result in a highly reversible Zn plating/striping process without visible dendrite growth. A MnO₂/CNFs || ZP-Zn full cell shows a high-capacity retention of 80.2 % after 1000 cycles with enhanced rate capability. Thereby, this modification method explored a novel way to supress zinc dendrite formation and effectively improves the electrochemical performance of AZBs.

4. Experimental Section

4.1 Synthesis of ZP- Zn electrode and MnO₂/CNFs positive electrode material

Figure S8 illustrates the preparation of the ZP-Zn electrode. 40 μL of 1.2 wt.% phytic acid solution, prepared by diluting the 50 wt.% PA aqueous solution (Sigma Aldrich; CAS: 83-86-3), was first dropped into the cathode side of a 2032 coin cell case. Then, a Zn disc (\emptyset = 12 mm; 50 μm thickness; Grillo) was put on the solution and maintained for 15 mins, during which the bottom side of the disc was etched by PA and a ZP layer was formed on the surface of it. This PA modified Zn disc is further named as ZP-Zn electrode. In order to confirm the formation of zinc phytate, the ZP power was also synthesized through the complexation reaction between zinc acetate dihydrate (98%; CAS: 5970-45-6; Sigma Aldrich) and 50% PA solution.

The MnO₂/carbon nanofibers (CNFs) composite, used as the positive electrode material in this work, was prepared *via* a hydrothermal reaction^[19]. 1.5 mmol MnSO₄·H₂O (99%; Carl Roth) was dissolved in 45 mL distilled water together with 1 mL 0.5 mol L⁻¹ H₂SO₄ solution, followed by adding 60 mg carbon nanofibers (CNFs, 100 nm × 20-200 μm, Sigma Aldrich). Then, 10 mL 0.1 mol L⁻¹ KMnO₄ (99%, Sigma Aldrich) solution was dropwise added under continuous stirring for 1 h. The hydrothermal reaction was carried out at 120 °C for 12 h in a Teflon-lined stainless-steel autoclave, and the dark precipitate was collected afterwards by centrifugation and washed three times with distilled water. The MnO₂/CNFs material was finally obtained after drying this precipitate at 80 °C

overnight. According to thermal gravimetric analysis (TGA, Q5000-lR, New Castle, USA), which is shown in **Figure S9**, the content of MnO₂ in MnO₂/CNFs composites is about 60%.

4.2 Material characterization

The surfaces of both bare Zn and ZP-Zn electrodes before and after Zn plating were characterized by scanning electron microscopy (SEM, Carl Zeiss AURIGA, Carl Zeiss Microscopy GmbH), the corresponding energy dispersive spectrometer (EDS) mapping was applied to analyse the element distribution. X-ray diffractometer (Bruker D8 Advance X-ray, Bruker) with Cu K α radiation (λ = 0.15418 nm) and attenuated total reflectance Fourier-Transform infrared spectroscopy (ATR-FTIR, Bruker Vertex 70) were used to characterize the structure of different samples.

4.3 Electrochemical measurements

4.3.1 Symmetric Zn | ZnSO₄+MnSO₄ | Zn cells

The Zn || Zn and ZP-Zn || ZP-Zn symmetric cells were assembled in two-electrode [22] 2032 coin cells with either glass fiber fleece (Whatman GF/D, \emptyset = 16 mm). Besides, in order to get a clear observation of SEM, filter paper (Whatman 540, \emptyset = 16 mm) also was used as separator in the cells that need to be dissembled, because glass fiber very easily attach on cycled electrodes and cover up which real morphology. 2 mol L⁻¹ ZnSO₄ (99%; Sigma Aldrich) and 0.2 mol L⁻¹ MnSO₄ aqueous solution (99%; Carl Roth) was used as electrolyte. The galvanostatic cycling at different plated capacities (0.05-0.5 mAh cm⁻²) under the current density of 0.25 mA cm⁻² was carried out on MACCOR series 4000 battery tester (Maccor Inc.). Electrochemical impedance spectroscopy (EIS) was recorded by VMP3 (BioLogic Science Instruments) in a frequency range of 100 kHz to 10 mHz. 4.3.2 $MnO_2/CNFs$ |ZnSO₄+MnSO₄| Zn full cells

Full cells were also assembled in 2032 coin cells with Zn metal (Zn or ZP-Zn) and MnO₂/CNFs as negative and positive electrode, and glass fiber (Whatman GF/D) as separator, respectively. The positive electrode was composed of MnO₂/CNFs active materials, Super C65 (conductive carbon, Imerys Graphite & Carbon) and polyvinylidene fluoride binder PVdF (Kynar Flex 761A, Arkema Group) with the ratio of 80:10:10 (*wt*.%). N-methyl-2-pyrrolidone (NMP, 99%, Sigma Aldrich) was

used as solvent for electrode paste preparation and stainless-steel (opening mesh: 0.085 mm, FE248703, Goodfellow) was applied as current collector. The mass loading of the active material (MnO₂/CNFs) was 1.5 ± 0.2 mg cm⁻². For electrochemical studies, the same electrolyte was used as described above. The charge/discharge cycling was conducted on the MACCOR series 4000 battery at a specific current of 500 mA g⁻¹ in the voltage range of 0.9 - 1.8 V. The specific capacity is calculated based on the mass of MnO₂/CNFs. Cyclic voltammetry (CV) and EIS were performed on a VMP3 system.

Acknowledgements

The authors are grateful for the financial support from German Research Foundation (DFG, project Li 2916/2-1) and the European Union through the Horizon 2020 framework program for research and innovation within the projects "VIDICAT" (829145).

Keywords: Zinc phytate; Surface modification; Zn dendrite; Aqueous zinc batteries

References

- a) M. S. Whittingham, Chemical Reviews 2004, 104, 4271-4302; b) R. Schmuch, R. Wagner, G. Hörpel,
 T. Placke, M. Winter, Nature Energy 2018, 3, 267-278; c) M. Winter, B. Barnett, K. Xu, Chemical Reviews 2018, 118, 11433-11456.
- [2] a) P. Meister, H. Jia, J. Li, R. Kloepsch, M. Winter, T. Placke, *Chemistry of Materials* **2016**, *28*, 7203-7217; b) S. Dühnen, J. Betz, M. Kolek, R. Schmuch, M. Winter, T. Placke, *Small Methods* **2020**; c) S. Dühnen, J. Betz, M. Kolek, R. Schmuch, M. Winter, T. Placke, *Small Methods* **2020**, *4*, 2000039.
- [3] a) M.-C. Lin, M. Gong, B. Lu, Y. Wu, D.-Y. Wang, M. Guan, M. Angell, C. Chen, J. Yang, B.-J. Hwang, H. Dai, *Nature* 2015, 520, 324-328; b) J. Muldoon, C. B. Bucur, T. Gregory, *Chemical Reviews* 2014, 114, 11683-11720; c) M. Song, H. Tan, D. Chao, H. J. Fan, *Advanced Functional Materials* 2018, 28, 1802564; d) W. Sun, F. Wang, B. Zhang, M. Zhang, V. Küpers, X. Ji, C. Theile, P. Bieker, K. Xu, C. Wang, *Science* 2021, 371, 46-51.
- [4] a) C. Xu, B. Li, H. Du, F. Kang, Angewandte Chemie 2012, 124, 957-959; b) N. Zhang, F. Cheng, Y. Liu,
 Q. Zhao, K. Lei, C. Chen, X. Liu, J. Chen, Journal of the American Chemical Society 2016, 138, 12894-12901; c) L. Kang, M. Cui, Z. Zhang, F. Jiang, Batteries & Supercaps 2020, 3, 966-1005.
- [5] a) L. E. Blanc, D. Kundu, L. F. Nazar, *Joule* **2020**; b) D. Selvakumaran, A. Pan, S. Liang, G. Cao, *Journal of Materials Chemistry A* **2019**, *7*, 18209-18236; c) M. Cui, Y. Xiao, L. Kang, W. Du, Y. Gao, X. Sun, Y. Zhou, X. Li, H. Li, F. Jiang, *ACS Applied Energy Materials* **2019**, *2*, 6490-6496.
- [6] H. Jia, Z. Wang, B. Tawiah, Y. Wang, C.-Y. Chan, B. Fei, F. Pan, *Nano Energy* **2020**, *70*, 104523.
- [7] a) R. Qin, Y. Wang, M. Zhang, Y. Wang, S. Ding, A. Song, H. Yi, L. Yang, Y. Song, Y. Cui, *Nano Energy* 2021, 80, 105478; b) Q. Zhang, J. Luan, Y. Tang, X. Ji, H. Wang, *Angewandte Chemie International Edition* 2020, 59, 13180-13191.

- [8] L. Kang, M. Cui, F. Jiang, Y. Gao, H. Luo, J. Liu, W. Liang, C. Zhi, *Advanced Energy Materials* **2018**, *8*, 1801090.
- [9] Z. Zhao, J. Zhao, Z. Hu, J. Li, Y. Zhang, C. Wang, G. Cui, *Energy & Environmental Science* **2019**, *12*, 1938-1949.
- [10] R. Yuksel, O. Buyukcakir, W. K. Seong, R. S. Ruoff, Advanced Energy Materials 2020, 10, 1904215.
- [11] a) X. Cui, Q. Li, Y. Li, F. Wang, G. Jin, M. Ding, *Applied Surface Science* **2008**, *255*, 2098-2103; b) X. Gao, C. Zhao, H. Lu, F. Gao, H. Ma, *Electrochim. Acta* **2014**, *150*, 188-196.
- [12] a) X. Cui, Y. Li, Q. Li, G. Jin, M. Ding, F. Wang, *Materials Chemistry and Physics* **2008**, *111*, 503-507; b) C. Sun, D. Xue, *Materials Research Innovations* **2013**, *18*, 370-375; c) C. Sun, D. Xue, *The Journal of Physical Chemistry C* **2013**, *117*, 19146-19153.
- [13] D. Yuan, W. Manalastas, L. Zhang, J. J. Chan, S. Meng, Y. Chen, M. Srinivasan, *ChemSusChem* **2019**, *12*, 4889-4900.
- [14] a) X. Guo, J. Zhou, C. Bai, X. Li, G. Fang, S. Liang, *Materials Today Energy* **2020**, *16*; b) L. Wang, W. Wu, W. Sun, Z. Yang, S. Wang, G. Liu, *Chemical Engineering Journal* **2019**, *373*, 8-22.
- [15] a) H. Pan, Y. Shao, P. Yan, Y. Cheng, K. S. Han, Z. Nie, C. Wang, J. Yang, X. Li, P. Bhattacharya, K. T. Mueller, J. Liu, *Nature Energy* **2016**, *1*; b) J. Huang, Z. Wang, M. Hou, X. Dong, Y. Liu, Y. Wang, Y. Xia, *Nat Commun* **2018**, *9*, 2906.
- [16] K. Zhao, C. Wang, Y. Yu, M. Yan, Q. Wei, P. He, Y. Dong, Z. Zhang, X. Wang, L. Mai, *Advanced Materials Interfaces* **2018**, *5*.
- [17] B. Lee, H. R. Seo, H. R. Lee, C. S. Yoon, J. H. Kim, K. Y. Chung, B. W. Cho, S. H. Oh, *ChemSusChem* **2016**, *9*, 2948-2956.
- [18] F. Wang, O. Borodin, T. Gao, X. Fan, W. Sun, F. Han, A. Faraone, J. A. Dura, K. Xu, C. Wang, *Nature Materials* **2018**, *17*, 543-549.
- [19] B. Wu, G. Zhang, M. Yan, T. Xiong, P. He, L. He, X. Xu, L. Mai, *Small* **2018**, *14*, e1703850.
- [20] Q. Zhang, J. Luan, L. Fu, S. Wu, Y. Tang, X. Ji, H. Wang, *Angew Chem Int Ed Engl* **2019**, *58*, 15841-15847.
- [21] a) M. H. Alfaruqi, V. Mathew, J. Gim, S. Kim, J. Song, J. P. Baboo, S. H. Choi, J. Kim, *Chemistry of Materials* **2015**, *27*, 3609-3620; b) W. Sun, F. Wang, S. Hou, C. Yang, X. Fan, Z. Ma, T. Gao, F. Han, R. Hu, M. Zhu, C. Wang, *Journal of the American Chemical Society* **2017**, *139*, 9775-9778.
- [22] R. Noelle, K. Beltrop, F. Holtstiege, J. Kasnatscheew, T. Placke, M. Winter, *Materials Today* **2020**, *32*, 131-146.